applied sciences

MDPI

*Article*

# Methane, Ethylene, and Ethane Detection by Differential Helmholtz Resonance Spectroscopy Using a 3345 nm Mid-Infrared Tunable Diode Laser Source

**Zhe Wu, Yunxing Shi and Yuwang Han ***

College of Chemistry and Molecular Engineering, Nanjing Tech University, Nanjing 210009, China
* Correspondence: hanyw@njtech.edu.cn; Tel.: +86-139-1399-6723

**Abstract:** Gas detection based on photoacoustic spectroscopy (PAS) has attracted extensive attention due to its high sensitivity and large range of linearity. Herein, to achieve the simultaneous detection of the light carbon gases ($CH_4$, $C_2H_4$, and $C_2H_6$), a gas detection system was constructed using a single mid-infrared tunable diode laser (central wavelength 3345 nm) source based on differential Helmholtz resonance spectroscopy (DHRS). The detection parameters (driving current, modulation depth, phase angle, etc.) were optimized under ambient pressure using the 1f demodulation method. With an integration time of 2 s, the detection limit reached 98.8 ppb, 252 ppb, and 33 ppb for methane, ethylene, and ethane, respectively. The validation test of the three-component mixture shows that the cross-interference can be effectively reduced by multiwavelength linear regression, and single wavelength linear regression causes large errors in the quantification of methane and ethylene.

**Keywords:** photoacoustic spectroscopy (PAS); multicomponent detection; interband cascade laser (ICL); Helmholtz resonance



**Citation:** Wu, Z.; Shi, Y.; Han, Y. Methane, Ethylene, and Ethane Detection by Differential Helmholtz Resonance Spectroscopy Using a 3345 nm Mid-Infrared Tunable Diode Laser Source. *Appl. Sci.* **2023**, *13*, 3169. https://doi.org/10.3390/app13053169

Academic Editor: Giulio Nicola Cerullo

Received: 2 February 2023
Revised: 26 February 2023
Accepted: 27 February 2023
Published: 1 March 2023



## 1. Introduction

Photoacoustic spectroscopy (PAS) is being actively developed in recent years, especially in trace gas detection [1]. As an indirect detection method based on absorption spectrum, PAS has the advantages of high detection sensitivity, good selectivity, fast detection speed, long service life [2], etc. It has been widely used in atmospheric research [3], medicine [4], the food industry [5], pollutant monitoring [6], and the power industry [7,8]. In many scenarios, single gas detection cannot meet the needs of practical applications, and the simultaneous monitoring of multiple components is indispensable. The selection of light source is the most important element in multicomponent detection based on PAS. Commonly used light sources include low-cost mid-infrared lamps equipped with ultranarrow band filters [9–11] and single-wavelength laser arrays [12–15]. These two devices need mechanical or optical accessories to accomplish wavelength switching. A more convenient alternative is to use a continuously tunable laser that covers the absorption wavelength of multiple gases [16]. For example, ethylene, acetone, and ammonia were detected in patient breath using $CO_2$ gas lasers [17]. Popa et al. used a $CO_2$ laser PAS system to measure five components, i.e., carbon dioxide, ammonia, ethanol, methanol, and ethylene [18]. In 1994, Faist et al. invented the quantum cascade laser (QCL) [19]. Due to its wide tunable wavelength range, QCL brought new possibilities for the development of PAS. Ma et al. used DFB-QCL with a center wavelength of 4610 nm as the laser source to detect CO and $N_2O$ in the tuning range of the absorption line with high sensitivity [20]. However, QCL has problems, such as the need for a large threshold current, in operation. To solve these problems, Yang [21] first reported the concept of a type II interband cascade laser (ICL). Unlike conventional semiconductor lasers, the active region of an ICL is connected in series, and this structure allows each injected electron to be reused at forward bias to emit multiple photons so that multiple gases can be detected simultaneously by a single laser when the

wavelength modulation method is employed. The simultaneous measurement of methane, ethane, and propane was accomplished using a quartz-enhanced PAS (QEPAS) sensor equipped with a single ICL with a central wavelength of 3345 nm [22].

In addition to the laser source, the photoacoustic cell and pressure sensor are also important factors affecting the detection performance of PAS. Longitudinal resonance and Helmholtz resonance photoacoustic cells are usually equipped with condenser microphones. Quartz tuning forks and cantilever beams are two highly sensitive pressure sensors that are used in conjunction with a specific structure of the cell. Because the quartz tuning fork enhanced photoacoustic spectrum has a higher quality factor Q and a higher resonance frequency, it can effectively reduce low-frequency noise [23] and work at a lower pressure, which is beneficial to reducing collision broadening. However, due to the tiny arm space of the tuning fork, beam collimation is very difficult [24]. Although the cantilever sensor has higher sensitivity than the traditional capacitive microphone [25], the temperature- and vibration-sensitive features of the interferometer become important issues [26]. Helmholtz resonance photoacoustic spectroscopy has high practical application value due to its relative simplicity and low cost [27,28]. The Helmholtz resonator is acoustically similar to a mechanical oscillator composed of two mass blocks and springs. The capillary tube connects two identical channels of the photoacoustic cell. The gas in the capillary tube moves like a piston at the resonance frequency, compressing the gas in one channel and releasing it in the other channel. Although only one unit of the photoacoustic cell is irradiated by the laser, at Helmholtz resonance frequency, both units in the DHR generate acoustic signals of the same size and opposite phase. It reduces non-resonant noise and has low requirements for light beam manipulation [29]. In particular, the two arms of the resonance tube can be used as measuring channels and/or reference channels and share a locking amplification module, which is particularly beneficial to multicomponent detection.

The simultaneous detection of trace ethylene and low carbon alkanes has many important applications. Examples include exhaled gas [30], agriculture, and dissolved gas analysis (DGA) in transformer oil [10]. In this paper, we used a differential Helmholtz resonance (DHR) [27,31–35] photoacoustic cell configured with condenser microphones and an ICL source to detect traces of $CH_4$, $C_2H_4$, and $C_2H_6$ under ambient pressure. These three components could be well quantified simultaneously by using a multiwavelength fitting algorithm to eliminate cross-interference.

## 2. Selection of Spectral Range

According to the standard absorption spectrum in the HITRAN database [36], methane, ethylene, and ethane have absorption signals in 3344–3350 nm, and this wavelength range can be covered by a single ICL laser. Therefore, this wavelength range can be selected for the simultaneous detection of the three gases. Methane has sharp absorption peaks between 3345.56 nm and 3345.83 nm, which are one order of magnitude stronger than those of ethylene and ethane. Ethane has absorption in the whole range of this band, with two absorption peaks at 3344.40 nm and 3348.19 nm. The absorption of ethylene is also dispersed over the whole band, and the maximum absorption at 3346.35 nm has obvious cross-talk with ethane and methane. Thus, appropriate measures need to be taken for the three-component mixture to minimize cross-interference.

## 3. Construction of the DHR Sensor

Considering the data in Figure 1, we chose the commercial Nanoplus ICL with a center wavelength of 3345 nm. The dynamic range of the ICL current is 20–100 mA, and the corresponding wavelength is 3344–3355 nm. The operating temperature is set at 20 °C with a typical output power of ca. 17.2 mW. The laser is driven with a lab-made circuit using the WTC3293 temperature control module (Wavelength Electronics, Bozeman, MT, USA). The ICL is mounted on a standard TO66 package equipped with a collimating lens. The outgoing spot is a beam 3 mm in diameter with Gaussian power distribution. The selected microphone is the full directional capacitive microphone (Shenzhen Yingge Acoustics

Technology Company, Shenzhen, China). The microphone has a sensitivity of −26 ± 3 dB. The DHR photoacoustic cell is made of 304 stainless steel (Figure 2). Both the main tubes and capillaries are 50 mm in length, and the inner diameters of them are 5 mm and 2 mm, respectively. The total volume of the photoacoustic cell is approximately 2.5 mL. Four calcium fluoride disks with a thickness of 0.5 mm are used as optical windows sealed at both ends of the two main tubes. Although only one main channel of the photoacoustic cell is illuminated by the laser at the Helmholtz resonance frequency, both channels produce acoustic signals of the same size in the opposite phase [27,28].

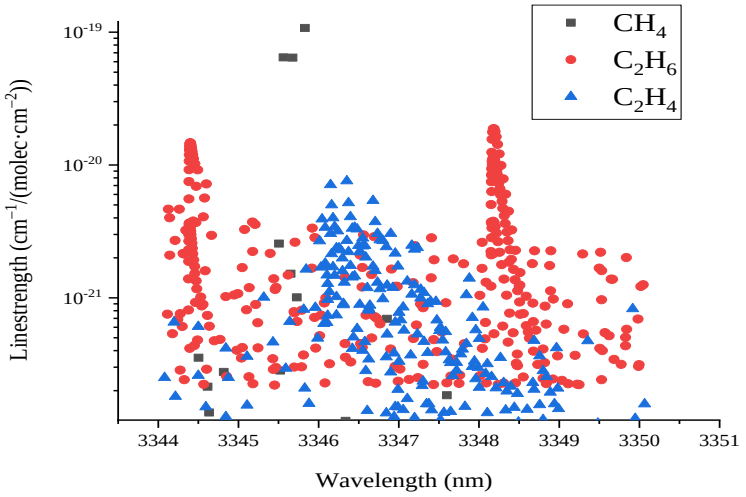


**Figure 1.** The line strengths of methane, ethylene, and ethane in 3344–3350 nm simulated using the HITRAN database.

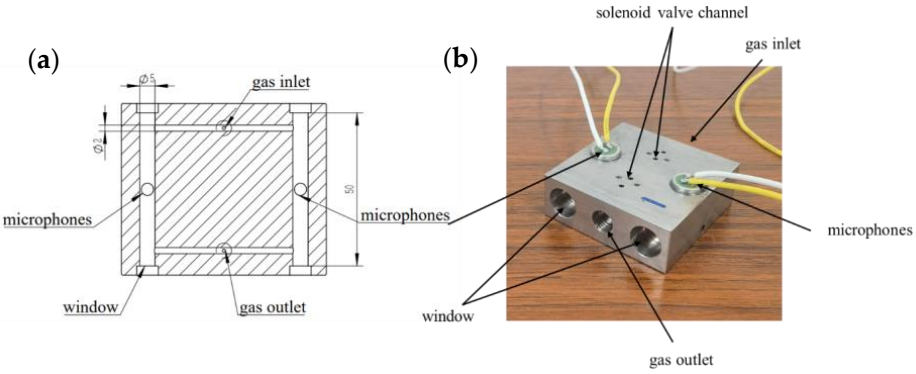


**Figure 2.** (**a**) Schematic and (**b**) photo of the DHR photoacoustic cell.

Figure 3 illustrates the procedure of gas detection. The sample gas with a certain concentration was prepared by mixing the standard gas (balanced with nitrogen) and high-purity nitrogen through two mass flowmeters. The photoacoustic cell was then purged with an excess of the sample gas to ensure that the photoacoustic cell was completely filled with the sample gas to be measured, and the pressure in the photoacoustic cell was controlled to ambient pressure. The ICL was wavelength-modulated by combing a triangle wave of 0.25 Hz and a sine wave at the cell resonance frequency. The amplitude of the triangle wave was 40–100 mA, i.e., the absorption wavelengths of the three sample gases were all covered with a complete scan. The signal acquisition was accomplished by the two microphones on the two channels. The signals were differentially amplified by a preamplifier with a gain of 100 and passed onto the lock-in amplifier (OE 1022, Sine Scientific Instrument, Guangzhou, China). All the lock-in amplified data were obtained with an integration time of 10 ms, and the output signal was collected by the VK701 data acquisition board (Vkinging Electronics, Shenzhen, China).

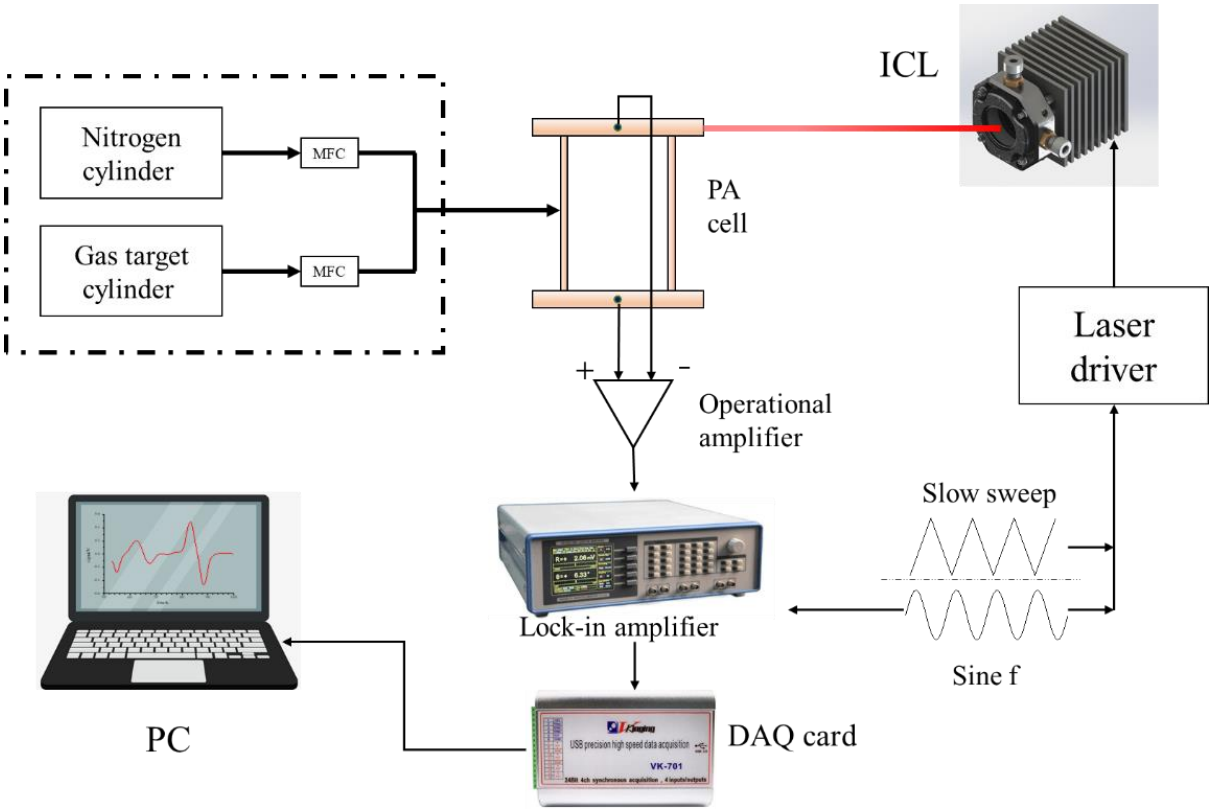


**Figure 3.** Schematic of the experimental workflow. (MFC: Mass flow controller; ICL: Interband cascade laser; PA cell: Photoacoustic cell; DAQ card: Data acquisition card; PC: Personal computer).

## 4. Optimization of Measurement Parameters

It is necessary to optimize the test conditions, such as laser modulation frequency, laser modulation depth, phase angle, and demodulation method, so that the best measurement conditions for the three different gases can be met at the same time.

### *4.1. Frequency and Depth of Laser Modulation*

We use the finite element software "COMSOL Multiphysics" to simulate the resonant frequency and obtain the calculated result of about 800 Hz. The frequency scan experiment shows that the resonance frequency is located at 710 Hz (Figure 4), and the quality factor is calculated to be Q = 6.70. Because the quality factor Q of the photoacoustic cell used in this paper is small, the frequency response curve is somewhat asymmetrical [37]. The distance between the two microphones located at the center of the two main tubes is far less than the wavelength of the acoustic wave at the resonance frequency (0.49 m). There is in-phase acoustical noise in each cell as the gas passes through both tubes identically, but this noise can be significantly suppressed by differentiating the signals of the measuring channel and the reference channel (Figure S1 and Table S1).

The amplitude of the laser modulation wave, i.e., the modulation depth, will directly affect the strength and the profile of the photoacoustic signal, and should be optimized experimentally.

In this paper, the photoacoustic signal of 57 ppm methane at different modulation depths is measured at the resonance frequency (710 Hz) of the photoacoustic cell, as shown in Figure 5.

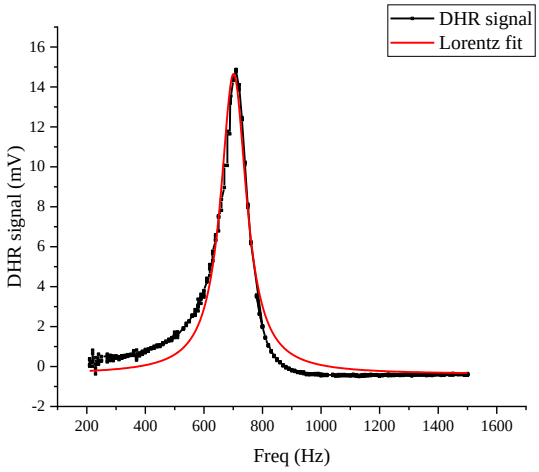


**Figure 4.** Frequency response of the DHR photoacoustic cell (50 ppm methane under ambient pressure).

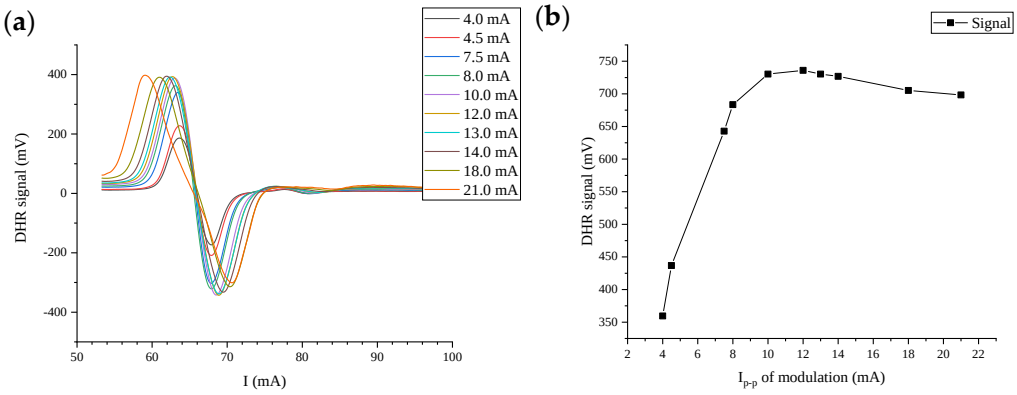


**Figure 5.** (**a**) Injection current scanning profile; (**b**) Variation of the 1f signal with the modulation depth.

It can be seen from Figure 5b that when the modulation depth is low, the photoacoustic signal increases with the increase of depth, reaches the maximum value when the amplitude is 12 mA, and then begins to decline slowly. This is because the modulation depth will affect the instantaneous power of the laser, and the greater the amplitude, the greater the output power. However, when the modulation depth is too large, wavelength shift and spectral line broadening will occur, as shown in Figure 5a. When the modulation depth is 10 mA, there is not much difference (>99%) with the maximum modulation depth of the signal at 12 mA (Figure 5b). Therefore, the modulation depth is comprehensively selected as 10 mA. Although the optimal modulation depth may depend on the gas molecules and pressure, for simplicity, we choose this value for all gases to be analyzed. It was demonstrated that ethane and ethylene can also show sufficient signal intensity at this modulation depth and meet the experimental requirements.

### *4.2. Demodulation Method*

To determine the detection current of each component, the absorption lines of the three gases in the full dynamic range of the ICL are investigated (Figure 6). At an ICL temperature of 20 °C, the injected current is modulated at the resonance frequency (710 Hz), and the resulting DHR photoacoustic signal is demodulated at 1f (Figure 6a) and 2f (Figure 6b). The background signal is collected with high purity nitrogen, and the final signal is obtained by subtracting the background signal from the sample gas signal. The study shows that when 2f demodulation is used, the response signals of ethylene and methane are almost in reversed phase (blue and violet regions in Figure 6b), which will cancel each other and is very unfavorable for detection. However, with the 1f demodulation mode, although the signals

of $CH_4$ and $C_2H_4$ also cancel each other in the injection current range of 69.5–71.4 mA (blue region in Figure 6a), a detection window arises for ethylene when the injection current is at 73.35–79.83 mA (violet region in Figure 6a). Thus, the demodulation method with 1f is adopted for signal acquisition. Since the first harmonic signal is affected by the residual amplitude modulation (RAM), the RAM will produce a background signal with a superimposed absorption signal, which is different from the second harmonic (without background signal), and the working curve will have a nonnegligible intercept [38].

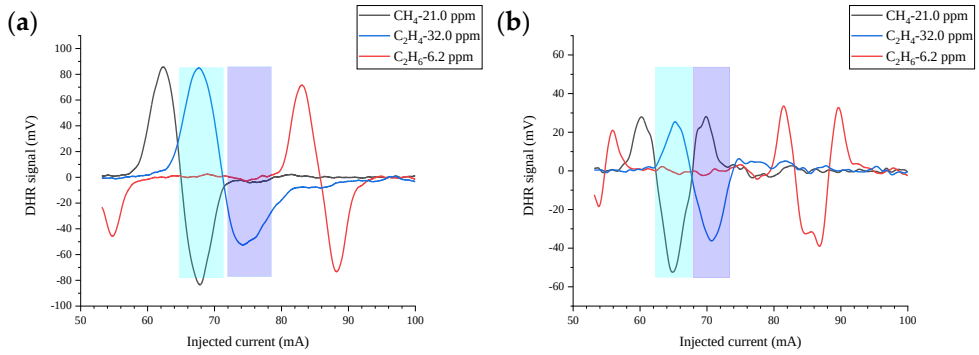


**Figure 6.** (**a**) 1f and (**b**) 2f signals of the three analytes in the full dynamic range of the ICL current (50 to 100 mA).

### *4.3. Phase Angle*

The lock-in amplifier is an important tool for detecting photoacoustic signals as it can extract weak signals from noisy backgrounds and measure them accurately. A certain phase difference exists between the detected signal and the original reference signal because of (1) the relaxation of exited gas molecules, (2) the energy loss due to the friction of the photoacoustic cell wall, and (3) the hysteresis of the electronic circuit. The phase difference θ of the lock-in amplifier should therefore be adjusted to maximize the signal. Figure 7 plots the signal of 50 ppm methane recorded by scanning the laser injection current at varying phase angles. With the given experimental conditions, the signal at a current value of 62.35 mA is well fitted with a cosine function and reaches a maximum when the phase angle is 12.1°. In addition, the phase angles of the other two gases (ethylene and ethane) are very close to that of methane when the maximum signal is reached. Therefore, for simplicity, the detection phase angle is set at 12.1° throughout the whole scanning process for all three gases.

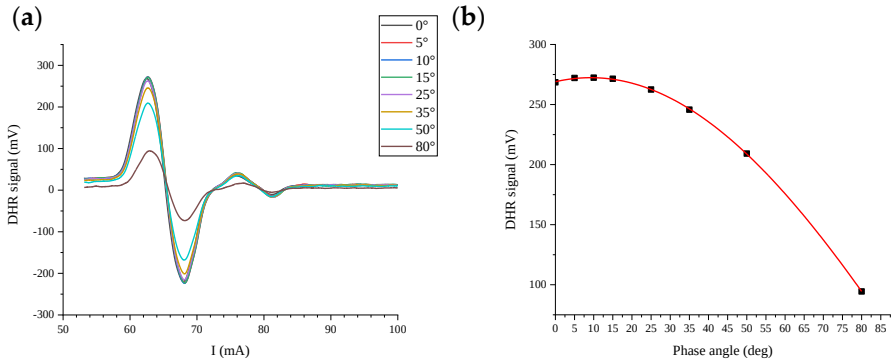


**Figure 7.** (**a**) First harmonic signals of 50 ppm methane under atmospheric pressure obtained at different phase angles; (**b**) cosine function fitting of the signal at an injected current of 62.57 mA.

## 5. Detection of Pure Methane, Ethylene, and Ethane

The photoacoustic sensor was calibrated under the optimized experimental conditions described above. The results show that the line broadening is so pronounced at atmospheric

pressure that the three absorption peaks/lines of methane are no longer distinguishable (Figure 6). At a current of $I$ = 64.81 mA, the laser emission wavelength corresponds to the absorption of $CH_4$ at 3345.68 nm, and the laser currents of $I_1$ = 62.35 mA and $I_1'$ = 67.81 mA correspond to the two peaks of its first harmonic. Because the absorption of $CH_4$ at current $I_1'$ has a large overlap with the absorption of $C_2H_4$, and the signals cancel each other, the signal at a current of $I_1$ is selected for the extraction of methane concentration. According to the data in the HITRAN database (Figure 1), $C_2H_4$ does not have a relatively sharp peak with high line strength in this band, but exhibits a broad band, and its first harmonic presents an asymmetric line type. $C_2H_6$ has two absorption peaks at 3344.40 nm and 3348.19 nm, and the former has a weaker absorption intensity. To obtain a longer laser wavelength in ICL, a larger injected current is needed, and as a result, the laser power output is higher and the obtained DHR photoacoustic signal is stronger. Hence, detecting $C_2H_6$ near 3348.19 nm is a better choice [22]. To reduce cross-interference, the detection current of $C_2H_4$ is selected as $I_2$ = 73.88 mA, and the detection current of $C_2H_6$ is selected as $I_3$ = 88.23 mA.

Methane sample gas with a concentration of 5–80 ppm was prepared by diluting a certified gas of 507 ppm methane in $N_2$ with high-purity nitrogen. Figure 8a shows the 1f signal of methane at different concentrations. At the selected methane detection laser current, $I$ = 62.35 mA, the signal values under different concentrations are then taken to generate the working curve. The data show that the signal of methane under this laser current has a good linear relationship (Figure 8b), and a responsivity of 4.953 mV/ppm can be derived from the linear fit. The Allan bias analysis shows (Figure 8c,d) that the detection limit of methane is ca. 98.8 ppb for a 2 s integration time, which is comparable to the QEPAS detection limit obtained under 200 Torr for a 1 s integration time [22].

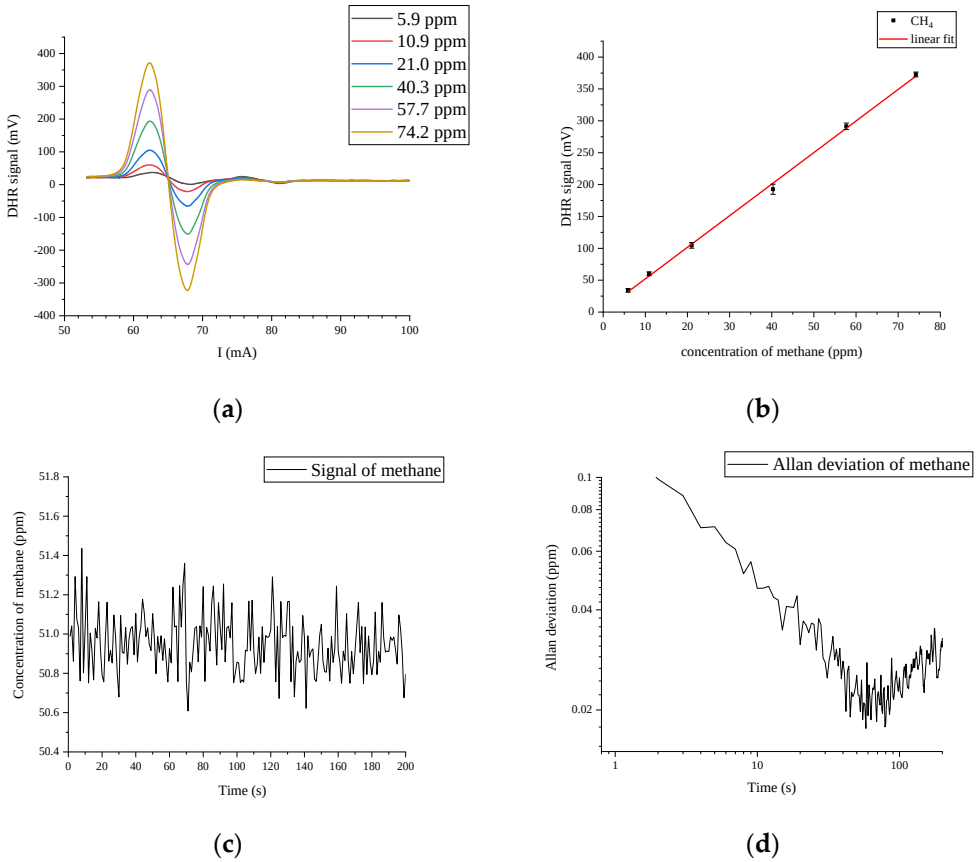


**Figure 8.** (**a**) First harmonic signals of methane (5 to 80 ppm) with the injected laser current in the range of 53 to 100 mA; (**b**) Linear fit of methane absorption peak at $I$ = 62.35 mA; (**c**) Continuous measurement 51.0 ppm methane; (**d**) The Allan deviation analysis.

For ethylene, the standard substance 401 ppm gas was used as the sample gas, and high-purity nitrogen was used as the dilution gas. Figure 9 shows the ethylene concentration gradient scan from 5 to 85 ppm. At the selected ethylene detection laser current, $I_2$ = 73.88 mA, the signal values of different concentrations are taken to draw the working curve. The data in the figure show that the signal response values of ethylene under this laser current have a good linear relationship, and the responsivity of the photoacoustic signal to the gas concentration is −1.778 mV/ppm. The Allan bias analysis shows (Figure 9c) that the lowest detectable concentration for ethylene detection is 252 ppb for an integration time of 2 s.

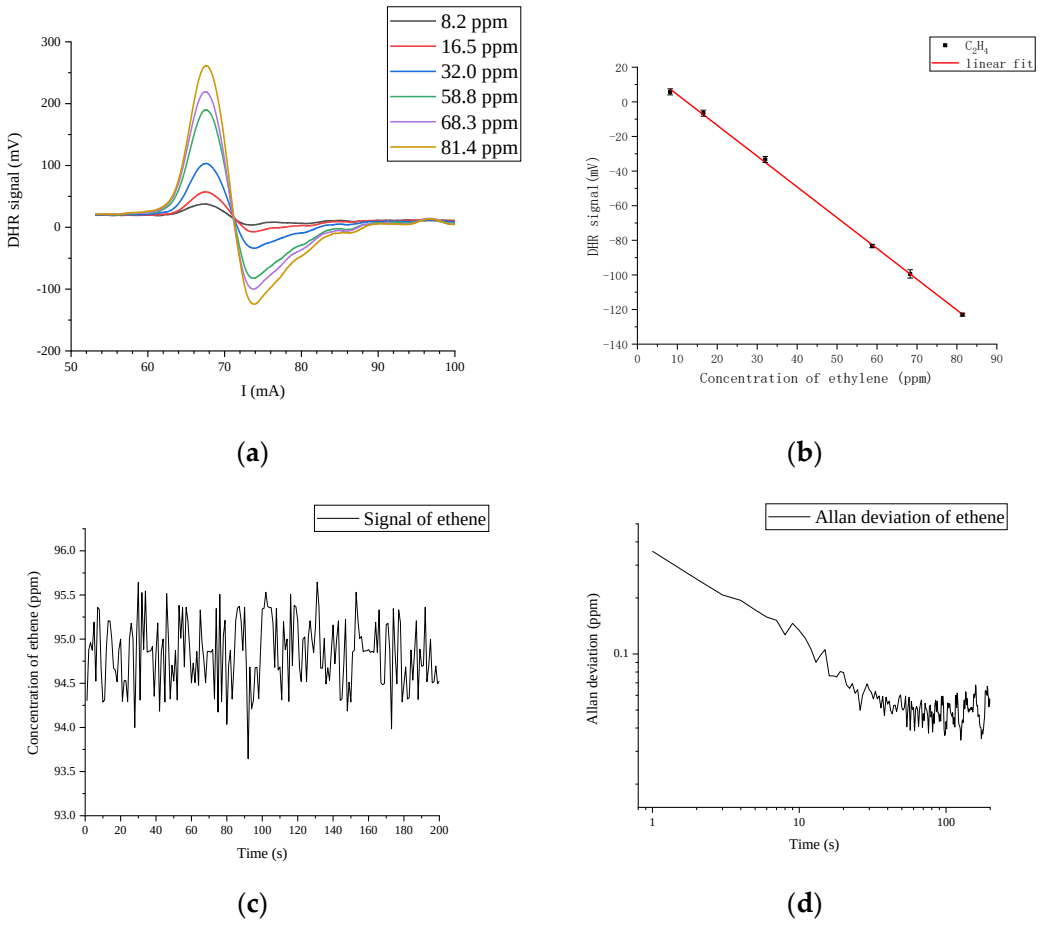


**Figure 9.** (**a**) The 1f signals of ethylene (5 to 85 ppm) at ambient pressure with the laser current in 53–100 mA; (**b**) Linearity of the 1f signal of ethylene obtained at $I_2$ = 73.88 mA; (**c**) Continuous measurement 95.0 ppm ethylene; (**d**) The Allan deviation analysis.

For ethane, the standard 207 ppm gas was used as the sample gas, and high purity nitrogen was used as the dilution gas. Figure 10 shows the ethane concentration gradient scan from 2 to 90 ppm. At the selected ethane detection laser current, $I_3$ = 88.23 mA, the signal values of different concentrations are taken to draw the working curve. The data in the figure show that the signal response values of ethane under this laser current have a good linear relationship, and the responsivity of the photoacoustic signal to the gas concentration is −13.78 mV/ppm. The Allan deviation analysis shows (Figure 10c) that the lowest detectable concentration for ethane detection is 33 ppb for an integration time of 2 s.

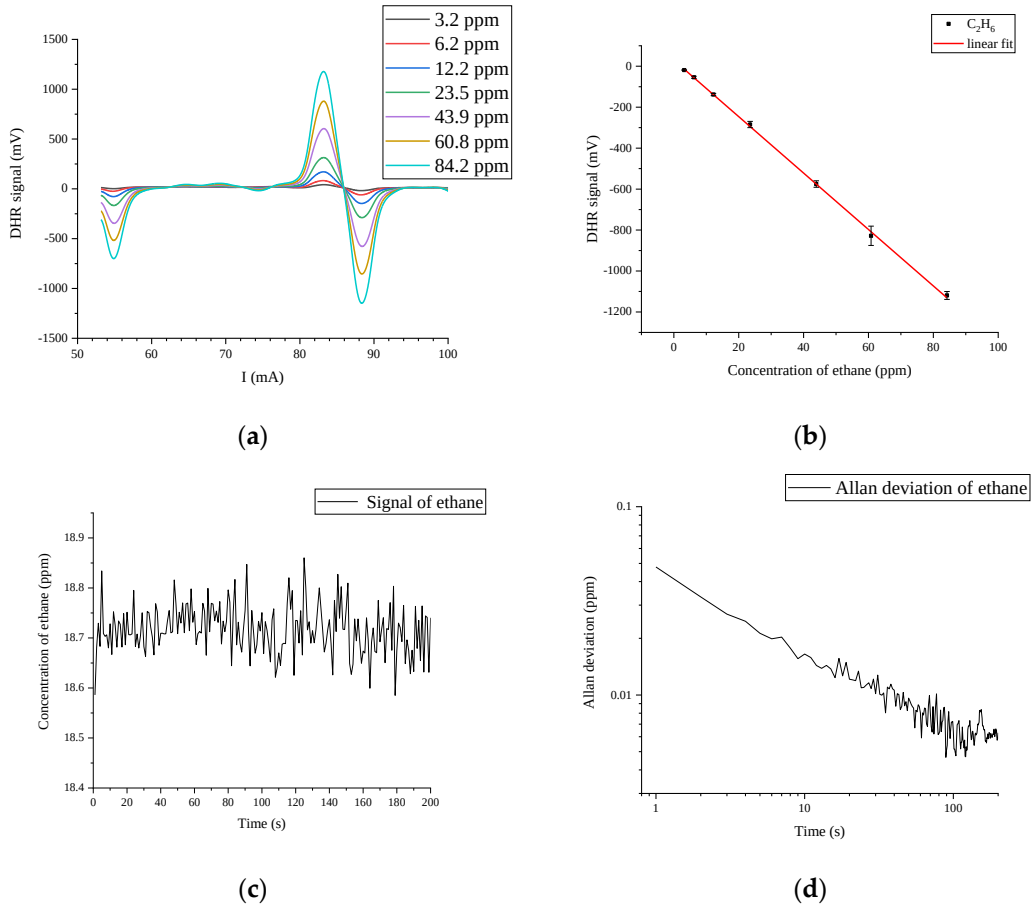


**Figure 10.** (**a**) First harmonic signals of ethane (2 to 90 ppm) with the laser current in the range of 53 to 100 mA; (**b**) Linear fit of ethane absorption peak at $I_3$ = 88.23 mA; (**c**) Continuous measurement of 18.7 ppm ethane; (**d**) The Allan deviation analysis.

In summary, the above results show that ethane has the highest responsivity and ethylene has the lowest responsivity. Although the absorption intensity of methane is stronger than ethane, the absorption cross section of methane is far lower than that of ethane. On the other hand, the detection wavelength of ethane is longer than that of methane, and the corresponding injection current at its absorption wavelength is higher. That is, ethane is detected at higher laser power and with higher responsivity [22]. For ethylene, its absorption strength is the lowest, and the absorption peak shape is not sharp (1f derivative signal will be low), so the responsivity is the lowest.

## 6. Multi-Gas Analysis

In the multicomponent system, if the response signal of each component at wavelength λ (corresponding to the laser injection current $I$) is linear with its concentration, the photoacoustic signal Y($I$) of the mixture can be expressed as the linear superposition of the signal at this wavelength related to each gas:

$$S(I) = \sum_{i=1}^{n} A_i(I)C_i + B(I) = A_{CH_4}(I)C_{CH_4} + A_{C_2H_4}(I)C_{C_2H_4} + A_{C_2H_6}(I)C_{C_2H_6} + B(I) \quad (1)$$

where $S(I)$ is the DHR signal obtained at the laser injected current $I$ (in mV), $A_i(I)$ is the responsivity at current $I$ for gas $i$ (in mV/ppm), $C_i$ is the concentration of gas $i$ (in ppm), and $B(I)$ is the background signal (in mV). We prepared seven different gas mixtures; the mixed gas sample is prepared in two ways. One is to dilute a bottle of high-concentration mixture with nitrogen. The high-concentration mixture contains three gases, and their

concentrations are close to each other. The first four mixtures were prepared by this method. The other way is to dilute three separate bottles of high-concentration single standard gas with nitrogen so that the concentration of each gas obtained can be changed at will. Three samples were prepared this way and the concentration difference between components is set to 3–5 times. The gas-dispensing, inflation, and measurement operations of each sample were repeated three times, and the test results are taken as the average value. The concentration of each component of the mixture is calculated by linear regression using both the single wavelength data and the multiwavelength data. Table 1 lists the responsivity and signal-concentration linearity ($R^2$) at the corresponding absorption peak of the three gases. Table 2 gives the nominal concentration of each component and the concentrations retrieved by the two regression procedures.

**Table 1.** Sensitivities (mV/ppm) and linearity ($R^2$) of single wavelength linear regression at the peak wavelengths (injection currents) for methane, ethylene, and ethane.

| | $I_1$ (62.35 mA) | | $I_2$ (73.88 mA) | | $I_3$ (88.33 mA) | |
|---|---|---|---|---|---|---|
| | **Slope** | **$R^2$** | **Slope** | **$R^2$** | **Slope** | **$R^2$** |
| $CH_4$ | 4.953 | 0.999 | −0.130 | 0.972 | −0.00622 | 0.822 |
| $C_2H_4$ | 0.232 | 0.999 | −1.778 | 0.999 | −0.125 | 0.953 |
| $C_2H_6$ | −0.038 | 0.964 | −0.355 | 0.999 | 13.780 | 0.999 |

**Table 2.** Nominal and calculated concentrations of the gas mixtures (SWLR: single wavelength linear regression, MWLR: multiple wavelength linear regression, Error = ($C_{Calculated} - C_{Norminal}$)/$C_{Norminal}$ * 100%).

| **Mixture No.** | **Nominal $CH_4$ Concentration [ppm]** | **Nominal $C_2H_4$ Concentration [ppm]** | **Nominal $C_2H_6$ Concentration [ppm]** | **Calculated $CH_4$ Concentration [ppm]** | | **Calculated $C_2H_4$ Concentration [ppm]** | | **Calculated $C_2H_6$ Concentration [ppm]** | |
|---|---|---|---|---|---|---|---|---|---|
| | | | | **SWLR Error** | **MWLR Error** | **SWLR Error** | **MWLR Error** | **SWLR Error** | **MWLR Error** |
| 1 | 6.11 | 6.37 | 6.37 | 5.25<br>−14.1% | 6.27<br>2.6% | 5.32<br>−16.5% | 6.09<br>−4.4% | 6.99<br>9.7% | 6.62<br>3.9% |
| 2 | 13 | 13 | 13 | 11.01<br>−15.3% | 12.75<br>−1.9% | 10.11<br>−22.2% | 11.7<br>−10.0% | 12.74<br>−2.0% | 13.17<br>1.3% |
| 3 | 29.9 | 30.0 | 30.1 | 27.66<br>−7.5% | 29.79<br>−0.4% | 32.37<br>7.9% | 32.75<br>9.2% | 29.64<br>−1.5% | 28.98<br>−3.7% |
| 4 | 53.3 | 53.5 | 53.7 | 52.02<br>−2.4% | 52.33<br>−1.8% | 52.28<br>−2.3% | 57.55<br>7.6% | 56.36<br>5.0% | 56.21<br>4.7% |
| 5 | 49 | 47.6 | 11.4 | 47.60<br>−2.9% | 49.35<br>0.7% | 45.08<br>−5.3% | 47.44<br>−0.3% | 10.52<br>−7.7% | 10.84<br>−4.9% |
| 6 | 11.9 | 47.5 | 34.3 | 10.65<br>−10.5% | 10.85<br>−8.8% | 41.97<br>−11.6% | 47.76<br>0.5% | 35.66<br>4.0% | 35.11<br>2.4% |
| 7 | 44.9 | 15.7 | 34.9 | 43.69<br>−2.7% | 40.66<br>−9.4% | 9.37<br>−40.3% | 14.87<br>−5.3% | 35.13<br>0.7% | 35.67<br>2.2% |

Ethane has a good absorption peak shape and the highest responsivity in this band. Furthermore, the signal at $I_3$ = 88.33 mA is basically not interfered with by the methane and ethylene signals (<1% interference). Therefore, even if the concentration of ethane is directly calculated from the working curve in Figure 9b, there will be no obvious error, and the relative error of all seven samples is less than ±10%. As mentioned above, in the case of a single component gas of methane, ethylene, or ethane, the absorption at right the peak and at wavelengths near the absorption peak show good linearity. However, when the absorption strength is small, the linear relationship far from the absorption peak worsens

(Table 1). When using single wavelength data for the linear solution, the calculated results of methane and ethylene have large errors in some cases because the cross-interference of ethane to ethylene reaches 20% (−0.3626/−1.778), and the interference of methane to ethylene is approximately 7.3%.

To reduce the impact of cross-interference on the detection accuracy, we carried out broadband multiwavelength linear regression through which the accidental error can be significantly reduced. Specifically, 20% of the scan data are evenly extracted in the whole dynamic range of the laser current (55–90 mA), and then the selected data with high concentration–signal linearity ($R^2$ > 0.99) are further chosen for multiwavelength fitting to obtain the gas concentrations through linear regression (Figure S2 and Table 2). The broadband scanning spectra of all mixed gases samples and the spectra fitted by linear regression verify that the multiwavelength correction method notably improves the detection accuracy. Taking the mixture 3 in Table 2 as an example, the contribution curves of each of the three different gases to the fitted spectra are shown in Figure 11a. The superimposed spectra are in good agreement with the measured spectrum of the mixture (residuals plot shown in Figure 11b). The detection error of ethylene and methane is reduced to less than ±10%, and the detection error of ethane is less than ±5%, which can meet practical application requirements (e.g., for DGA). In our subsequent research, we aim to further optimize the fitting process by introducing weight factors to different wavelengths or using machine learning methods to improve the detection performance.

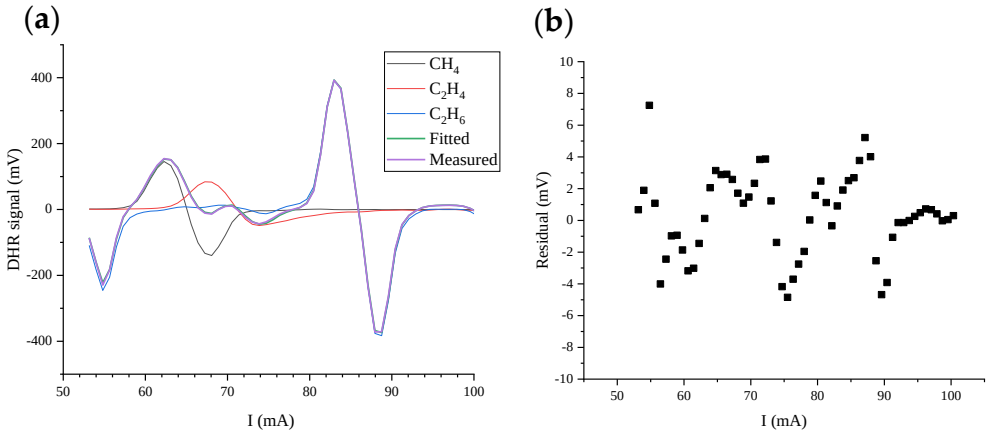


**Figure 11.** (**a**) Multi-wavelength fitting profiles of the mixture 3 in Table 2; (**b**) The fitting residual plot.

## 7. Conclusions

The simultaneous detection of methane, ethylene, and ethane is of great significance in the power industry, the petroleum industry, agriculture, and other fields. The photoacoustic sensor in this paper is constructed from a Helmholtz resonance cell equipped with a single ICL light source, and can simultaneously detect methane, ethylene, and ethane at normal pressure. With an integration time of 2 s, the detection limits of the sensor for methane, ethylene, and ethane can reach 98.8 ppb, 252 ppb, and 33 ppb, respectively. Due to the large-range cancellation of ethylene and methane 2f demodulation signals, the 1f demodulation with a certain detection window is applied. By fitting the multiwavelength data with the least squares method, the mutual interference in the three-component mixture is effectively reduced, and the concentrations of the three components are successfully and accurately derived. This Helmholtz resonance photoacoustic system has good stability and can effectively adapt to complex application environments. In the future, thanks to the special structure of the Helmholtz resonator, another laser can be directly added to another channel to further increase the number of types of gases that can be simultaneously detected without using auxiliary tools such as a beam combiner.

**Supplementary Materials:** The following supporting information can be downloaded at: https://www.mdpi.com/article/10.3390/app13053169/s1, Figure S1: PA cell left and right microphone signals and differential signals; Table S1: Average and standard deviation of the left and right microphone signals and differential signals; Figure S2: Broadband 1f spectra of the seven gas mixtures listed in Table 2 and their multi-wavelength fittings.

**Author Contributions:** Designed/modified the experimental setup and writing—original draft preparation, Z.W.; performed the experiments and analyzed the data, Z.W. and Y.S.; data curation, Z.W., Y.S. and Y.H.; writing—review and editing, Y.H. All authors have read and agreed to the published version of the manuscript.

**Funding:** This research received no external funding.

**Institutional Review Board Statement:** Not applicable.

**Informed Consent Statement:** Not applicable.

**Data Availability Statement:** The data underlying the results presented in this paper are not publicly available at this time, but may be obtained from the authors upon reasonable request.

**Acknowledgments:** The authors are grateful to Jianyuan Huang, Tianwei Wang and Weiping Kong for valuable discussion and help.

**Conflicts of Interest:** The authors declare no conflict of interest.

## References

1. Bozóki, Z.; Pogány, A.; Szabó, G. Photoacoustic Instruments for Practical Applications: Present, Potentials, and Future Challenges. *Appl. Spectrosc. Rev.* **2011**, *46*, 1–37. [CrossRef]
2. Wilcken, K.; Kauppinen, J. Optimization of a Microphone for Photoacoustic Spectroscopy. *Appl. Spectrosc.* **2003**, *57*, 1087–1092. [CrossRef] [PubMed]
3. Liu, Q.; Sun, Y.; Qiu, X.; Guo, G.; Li, L.; Gong, T.; Li, C. Resonant photoacoustic spectrometer enhanced by multipass absorption for detecting atmospheric $CH_4$ at the ppb-level. *Front. Chem.* **2022**, *10*, 1021145. [CrossRef] [PubMed]
4. Jin, Y.; Yin, Y.; Li, C.; Liu, H.; Shi, J. Non-Invasive Monitoring of Human Health by Photoacoustic Spectroscopy. *Sensors* **2022**, *22*, 1155. [CrossRef] [PubMed]
5. Hernández-Aguilar, C.; Domínguez-Pacheco, A.; Cruz-Orea, A.; Ivanov, R. Photoacoustic Spectroscopy in the Optical Characterization of Foodstuff: A Review. *J. Spectrosc.* **2019**, *2019*, 1–34. [CrossRef]
6. Liu, L.; Mandelis, A.; Melnikov, A.; Michaelian, K.; Huan, H.; Haisch, C. Step-Scan T-Cell Fourier Transform Infrared Photoacoustic Spectroscopy (FTIR-PAS) for Monitoring Environmental Air Pollutants. *Int. J. Thermophys.* **2016**, *37*, 64. [CrossRef]
7. Chen, Z.; Zhang, X.; Cheng, H.; Zhang, Y.; Yang, T.; Zhang, Y. Study on Photoacoustic Spectroscopy Detection of CO in Gas Insulation Equipment. *IEEE Trans. Dielectr. Electr. Insul.* **2022**, *29*, 1498–1505. [CrossRef]
8. Chen, K.; An, R.; Li, C.; Kang, Y.; Ma, F.; Zhao, X.; Guo, M.; Qi, H.; Zhao, J. Detection of ultra-low concentration acetylene gas dissolved in oil based on fiber-optic photoacoustic sensing. *Opt. Laser Technol.* **2022**, *154*, 108299. [CrossRef]
9. Gong, Z.; Chen, K.; Yang, Y.; Zhou, X.; Yu, Q. Photoacoustic spectroscopy based multi-gas detection using high-sensitivity fiber-optic low-frequency acoustic sensor. *Sens. Actuators B Chem.* **2018**, *260*, 357–363. [CrossRef]
10. Chen, K.; Zhang, B.; Guo, M.; Chen, Y.; Deng, H.; Yang, B.; Liu, S.; Ma, F.; Zhu, F.; Gong, Z.; et al. Photoacoustic trace gas detection of ethylene in high-concentration methane background based on dual light sources and fiber-optic microphone. *Sens. Actuators B Chem.* **2020**, *310*, 127825. [CrossRef]
11. Kuusela, T.; Peura, J.; Matveev, B.A.; Remennyy, M.A.; Stus, N.M. Photoacoustic gas detection using a cantilever microphone and III–V mid-IR LEDs. *Vib. Spectrosc.* **2009**, *51*, 289–293. [CrossRef]
12. Liu, K.; Mei, J.; Zhang, W.; Chen, W.; Gao, X. Multi-resonator photoacoustic spectroscopy. *Sens. Actuators B Chem.* **2017**, *251*, 632–636. [CrossRef]
13. Wu, H.; Yin, X.; Dong, L.; Pei, K.; Sampaolo, A.; Patimisco, P.; Zheng, H.; Ma, W.; Zhang, L.; Yin, W.; et al. Simultaneous dual-gas QEPAS detection based on a fundamental and overtone combined vibration of quartz tuning fork. *Appl. Phys. Lett.* **2017**, *110*, 121104. [CrossRef]
14. Huang, Q.; Wei, Y.; Li, J. Simultaneous detection of multiple gases using multi-resonance photoacoustic spectroscopy. *Sens. Actuators B Chem.* **2022**, *369*, 132234. [CrossRef]
15. Jiang, Y.; Zhang, T.; Wang, G.; He, S. A Dual-Gas Sensor Using Photoacoustic Spectroscopy Based on a Single Acoustic Resonator. *Appl. Sci.* **2021**, *11*, 5224. [CrossRef]
16. Yi, H.; Laurent, O.; Schilt, S.; Ramonet, M.; Gao, X.; Dong, L.; Chen, W. Simultaneous Monitoring of Atmospheric $CH_4$, $N_2O$, and $H_2O$ Using a Single Gas Sensor Based on Mid-IR Quartz-Enhanced Photoacoustic Spectroscopy. *Anal. Chem.* **2022**, *94*, 17522–17532. [CrossRef]

17. Mitrayana, N.; Nikita, J.G.; Wasono, M.A.J.; Satriawan, M. $CO_2$ laser photoacoustic spectrometer for measuring ethylene, acetone, and ammonia in the breath of patients with renal disease. *Sens. Bio-Sens. Res.* **2020**, *30*, 100387. [CrossRef]
18. Popa, C.; Bratu, A.M.; Petrus, M. A comparative photoacoustic study of multi gases from human respiration: Mouth breathing vs. nasal breathing. *Microchem. J.* **2018**, *139*, 196–202. [CrossRef]
19. Faist, J.; Capasso, F.; Sivco, D.L.; Sirtori, C.; Hutchinson, A.L.; Cho, A.Y. Quantum cascade laser. *Science* **1994**, *264*, 553–556. [CrossRef]
20. Ma, Y.; Lewicki, R.; Razeghi, M.; Tittel, F.K. QEPAS based ppb-level detection of CO and $N_2O$ using a high power CW DFB-QCL. *Opt. Express* **2013**, *21*, 1008–1019. [CrossRef]
21. Yang, R.Q. Infrared laser based on intersubband transitions in quantum wells. *Superlattice. Microst.* **1995**, *17*, 77–83. [CrossRef]
22. Sampaolo, A.; Csutak, S.; Patimisco, P.; Giglio, M.; Menduni, G.; Passaro, V.; Tittel, F.K.; Deffenbaugh, M.; Spagnolo, V. Methane, ethane and propane detection using a compact quartz enhanced photoacoustic sensor and a single interband cascade laser. *Sens. Actuators B Chem.* **2019**, *282*, 952–960. [CrossRef]
23. Petra, N.; Zweck, J.; Kosterev, A.A.; Minkoff, S.E.; Thomazy, D. Theoretical analysis of a quartz-enhanced photoacoustic spectroscopy sensor. *Appl. Phys. B* **2009**, *94*, 673–680. [CrossRef]
24. Zheng, H.; Lin, H.; Dong, L.; Huang, Z.; Gu, X.; Tang, J.; Dong, L.; Zhu, W.; Yu, J.; Chen, Z. Quartz-Enhanced Photothermal-Acoustic Spectroscopy for Trace Gas Analysis. *Appl. Sci.* **2019**, *9*, 4021. [CrossRef]
25. Koskinen, V.; Fonsen, J.; Roth, K.; Kauppinen, J. Progress in cantilever enhanced photoacoustic spectroscopy. *Vib. Spectrosc.* **2008**, *48*, 16–21. [CrossRef]
26. Zhang, X.; Liu, L.; Liu, Y.; Zhang, L.; Yin, X.; Huan, H.; Xi, T.; Shao, X. Detectors for gas-phase photoacoustic spectroscopy: A review. *Microw. Opt. Techn. Let.* **2022**, 1–10. [CrossRef]
27. Zéninari, V.; Parvitte, B.; Courtois, D.; Kapitanov, V.A.; Ponomarev, Y.N. Methane detection on the sub-ppm level with a near-infrared diode laser photoacoustic sensor. *Infrared Phys. Technol.* **2003**, *44*, 253–261. [CrossRef]
28. Mattiello, M.; Niklès, M.; Schilt, S.; Thévenaz, L.; Salhi, A.; Barat, D.; Vicet, A.; Rouillard, Y.; Werner, R.; Koeth, J. Novel Helmholtz-based photoacoustic sensor for trace gas detection at ppm level using GaInAsSb/GaAlAsSb DFB lasers. *Spectrochim. Acta Part A Mol. Biomol. Spectrosc.* **2006**, *63*, 952–958. [CrossRef]
29. Rouxel, J.; Coutard, J.; Gidon, S.; Lartigue, O.; Nicoletti, S.; Parvitte, B.; Vallon, R.; Zéninari, V.; Glière, A. Miniaturized differential Helmholtz resonators for photoacoustic trace gas detection. *Sens. Actuators B Chem.* **2016**, *236*, 1104–1110. [CrossRef]
30. Giubileo, G. Laser-based assessment of lipid peroxidation in humans. *Proc. SPIE-Int. Soc. Opt. Eng.* **1998**, *74*, 1658–1676.
31. Barbieri, S.; Pellaux, J.; Studemann, E.; Rosset, D. Gas detection with quantum cascade lasers: An adapted photoacoustic sensor based on Helmholtz resonance. *Rev. Sci. Instrum.* **2002**, *73*, 2458–2461. [CrossRef]
32. Fernelius, N.C. Helmholtz resonance effect in photoacoustic cells. *Appl. Optics* **1979**, *18*, 1784–1787. [CrossRef] [PubMed]
33. Starecki, T.; Geras, A. Differential Open Photoacoustic Helmholtz Cell. *Int. J. Thermophys.* **2014**, *35*, 2259–2268. [CrossRef]
34. Li, Z.; Liu, J.; Si, G.; Ning, Z.; Fang, Y. Design of a high-sensitivity differential Helmholtz photoacoustic cell and its application in methane detection. *Opt. Express* **2022**, *30*, 28984. [CrossRef] [PubMed]
35. Zeninari, V.; Kapitanov, V.A.; Courtois, D.; Ponomarev, Y.N. Design and characteristics of a differential Helmholtz resonant photoacoustic cell for infrared gas detection. *Infrared Phys. Techn.* **1999**, *40*, 1–23. [CrossRef]
36. Rothman, L.S.; Gordon, I.E.; Babikov, Y.; Barbe, A.; Chris Benner, D.; Bernath, P.F.; Birk, M.; Bizzocchi, L.; Boudon, V.; Brown, L.R.; et al. The HITRAN2012 molecular spectroscopic database. *J. Quant. Spectrosc. Radiat. Transf.* **2013**, *130*, 4–50. [CrossRef]
37. Miklós, A.; Hess, P.; Bozóki, Z. Application of acoustic resonators in photoacoustic trace gas analysis and metrology. *Rev. Sci. Instrum.* **2001**, *72*, 1937. [CrossRef]
38. Ruxton, K.; Chakraborty, A.L.; Johnstone, W.; Lengden, M.; Stewart, G.; Duffin, K. Tunable diode laser spectroscopy with wavelength modulation: Elimination of residual amplitude modulation in a phasor decomposition approach. *Sens. Actuators B Chem.* **2010**, *150*, 367–375. [CrossRef]